

## ELEMENTARY PARTICLES AND FIELDS

### Experiment

# Albedo in the ATIC Experiment: Measurements and Simulations

N. V. Sokolskaya<sup>1)\*</sup>, J. H. Adams, Jr.<sup>2)</sup>, H. S. Ahn<sup>3)</sup>, K. E. Batkov<sup>1)</sup>, G. L. Bashindzhagyan<sup>1)</sup>,  
J. Z. Wang<sup>3)</sup>, J. P. Wefel<sup>4)</sup>, J. Wu<sup>3)</sup>, O. Ganel<sup>3)</sup>, T. G. Guzik<sup>4)</sup>, R. M. Gunasingha<sup>5)</sup>,  
V. I. Zatsepin<sup>1)</sup>, J. Isbert<sup>4)</sup>, K. C. Kim<sup>3)</sup>, M. Christl<sup>2)</sup>, E. N. Kouznetsov<sup>1)</sup>, M. I. Panasyuk<sup>1)</sup>,  
A. D. Panov<sup>1)</sup>, E. S. Seo<sup>3)</sup>, A. R. Fazely<sup>5)</sup>, J. Chang<sup>6),7)</sup>, and W. K. H. Schmidt<sup>6)</sup>

Received April 28, 2004; in final form, September 8, 2004

**Abstract**—We analyze the characteristics of the albedo, or the backscatter current, which constitutes a background for charge measurements in calorimetric experiments in high-energy cosmic rays. We compare the experimental data obtained in the flights of the ATIC spectrometer with the simulations performed using the GEANT 3.21 code. We discuss the influence of the backscatter on the charge resolution in the ATIC experiment. © 2005 Pleiades Publishing, Inc.

## 1. INTRODUCTION

A number of experiments in which an ionization calorimeter was used to directly measure the spectra at high energies have been carried out to date. The experiments onboard the PROTON satellites [1] were performed in 1965–1968 first. However, the results obtained were inconclusive due to the possible signal distortion in the charge detector module by albedo particles from the calorimeter [2]. The albedo problem was completely solved in experiments with emulsion chambers owing to the high spatial resolution achieved in nuclear emulsion analysis. When applied to cosmic-ray studies, this technique has a number of shortcomings, namely, a high energy threshold and insufficient reliability of energy measurements. The technique is also very laborious. Therefore, the results obtained in three emulsion experiments differed significantly [3–5]. A successful method for solving the problem of the backscatter current was used in the SOKOL experiment [6], in which directional Cherenkov detectors were employed to determine the charges of light nuclei (protons and helium). Thin nondirectional Cherenkov counters were used to measure the charges of heavier nuclei. However, the

charge resolution in this experiment was too low for nuclei heavier than helium to be resolved.

A different method for significantly reducing the albedo influence on charge measurements was used in the ATIC experiment. This experiment is aimed at performing new measurements of the energy spectrum for galactic cosmic rays with an individual charge resolution from protons to iron over a wide energy range, from 100 GeV to 100 TeV per particle. A matrix of silicon detectors has been used for the first time to measure the charge. The albedo problem is solved here through the fine segmentation of the charge detector. The matrix design of the charge detector offers a possibility for studying the pulse and lateral albedo signal distributions as a function of energy and type of primary particles. Comparison of experimental data with simulations verifies whether the simulations can be used in situations where no experimental data can be obtained.

## 2. THE ATIC SPECTROMETER

The layout of the spectrometer is shown in Fig. 1. A fully active calorimeter built from 320 bismuth-germanate (BGO) scintillator crystals, each  $25 \times 2.5 \times 2.5$  cm in size, measures the energy of each cascade. The BGO crystals form eight layers, each  $50 \times 50$  cm in area, with the crystal axes lying alternately along the  $X$  and  $Y$  axes. The calorimeter depth is 18 radiation units. The target module consists of three 10-cm-thick graphite layers (density  $1.7 \text{ g cm}^{-3}$ ) and lies above the calorimeter. The target thickness, including the constructional materials and scintillators, is  $3/4$  of the proton interaction length.

<sup>1)</sup>Skobeltsyn Institute of Nuclear Physics, Moscow State University, Vorob'evy gory, Moscow, 119992 Russia.

<sup>2)</sup>Marshall Space Flight Center, NASA, Huntsville, AL, USA.

<sup>3)</sup>University of Maryland, College Park, MD, USA.

<sup>4)</sup>Louisiana State University, Baton Rouge, LA, USA.

<sup>5)</sup>Southern University, Baton Rouge, LA, USA.

<sup>6)</sup>Max Planck Institut für Aeronomie, Lindau, Germany.

<sup>7)</sup>Purple Mountain Observatory, Chinese Academy of Sciences, China.

\* e-mail: sok@dec1.sinp.msu.ru

The instrument has three hodoscopes built from 202 strips of plastic scintillators 1 cm thick and 2 cm wide. Each hodoscope consists of two mutually perpendicular strip layers. The hodoscopes are placed above, under, and inside the graphite target and form the first level trigger, which determines the aperture of the instrument, and provide additional measurements of the charge and trajectory of the primary particle reconstructed from the cascades in the calorimeter. The charge detector, a silicon matrix built from 4480 silicon pixels  $1.5 \times 2$  cm in size, is the uppermost detector in the instrument. The silicon pixels are arranged in four planes with a small overlap along the  $X$  and  $Y$  axes to avoid the holes through which the primary particle could pass. Thus, each particle inside the aperture of the instrument passes at least through one silicon pixel, and about 15% of the particles pass through two pixels. The total matrix area is  $99.2 \times 111.2$  cm. The ATIC silicon matrix and its properties are described in detail in [7, 8].

### 3. FLIGHTS IN THE STRATOSPHERE

ATIC was launched for its first test flight on December 28, 2000, at McMurdo, Antarctica. Having made a complete turn around the South Pole, it landed on January 13, 2001. The altitude of the flight was  $37 \pm 1.5$  km. Since ATIC landed successfully and was recovered in good condition, it could be flown again after refurbishment. The second, scientific, flight was also carried out in Antarctica from December 29, 2002, through January 18, 2003. A third flight is scheduled to increase the statistics, particularly at high energies. The goal of the ATIC-1 flight was to test the operation of all detectors and systems of the instrument. However, the first scientific data were obtained during this flight. We used ATIC-1 data to study the backscatter current and its influence on the charge resolution of the ATIC spectrometer.

### 4. RECONSTRUCTION OF EVENTS IN THE SPECTROMETER

Each high-energy event detected by the instrument is reconstructed from the signals in the detectors to determine the primary particle charge, energy,

**Table 1.** Trajectory reconstruction accuracy and mean size of the search area for events of various energies

$E_d$ , GeV	$\sigma_X$ , cm	$\sigma_Y$ , cm	Search area $\Delta X, \Delta Y$ , cm
>10	10.3	9.6	$\pm 30$
>100	4.6	4.6	$\pm 14$
>1000	2.7	3.2	$\pm 9$

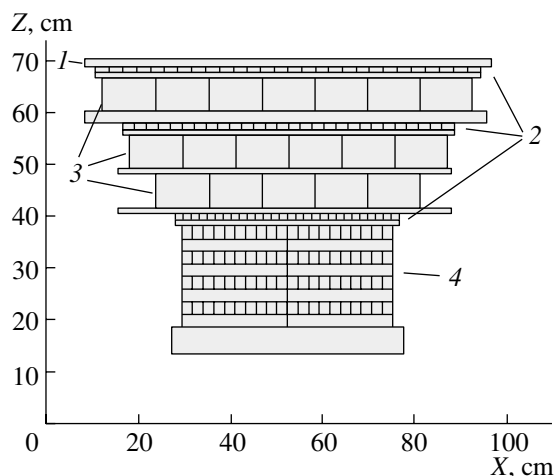


**Fig. 1.** Layout of the ATIC spectrometer: 1—silicon matrix, 2—scintillator hodoscopes, 3—graphite target, 4—BGO calorimeter.

and trajectory in the instrument. The particle trajectory was reconstructed from the signals in the BGO calorimeter and was described by two projections in the  $XZ$  and  $YZ$  planes (see Fig. 2). Both projections are reconstructed independently using the  $Y$ - and  $X$ -oriented crystal layers, respectively. The crystal with the maximum energy deposition is determined in each layer. (If this crystal is found near the edge of the layer, then the event is considered to be a side event and is rejected.) Subsequently, the symmetrized weight center of the energy distribution in the layer is found by taking into account the crystals in both directions from the central crystal. The dispersions of the weight centers are determined from simulated cascades (see below): in each layer, the dispersion of the location of the weight center is determined as a function of the energy deposition in the layer. The parameters of the trajectory projections onto the  $XZ$  and  $YZ$  planes and their  $\chi^2$  values are calculated using these weight centers in the  $X$ - and  $Y$ -oriented layers of the

**Table 2.** Probability of an albedo signal with  $Q > 1.5$  (for protons) and  $Q > 2.5$  (for helium nuclei) in various regions around the point of incidence of the primary particle (in %)

Search area	Protons			Helium		
	$E_d$ , GeV			$E_d$ , GeV		
$\Delta X, \Delta Y$ , cm	>10	>100	>1000	>10	>100	>1000
$\pm 5$	0.6	0.6	1.6	0.1	0.15	0.7
$\pm 10$	1.7	2.2	6.3	0.1	1	2.2
$\pm 25$	5.6	13.6	37.6	0.8	2.8	8.4

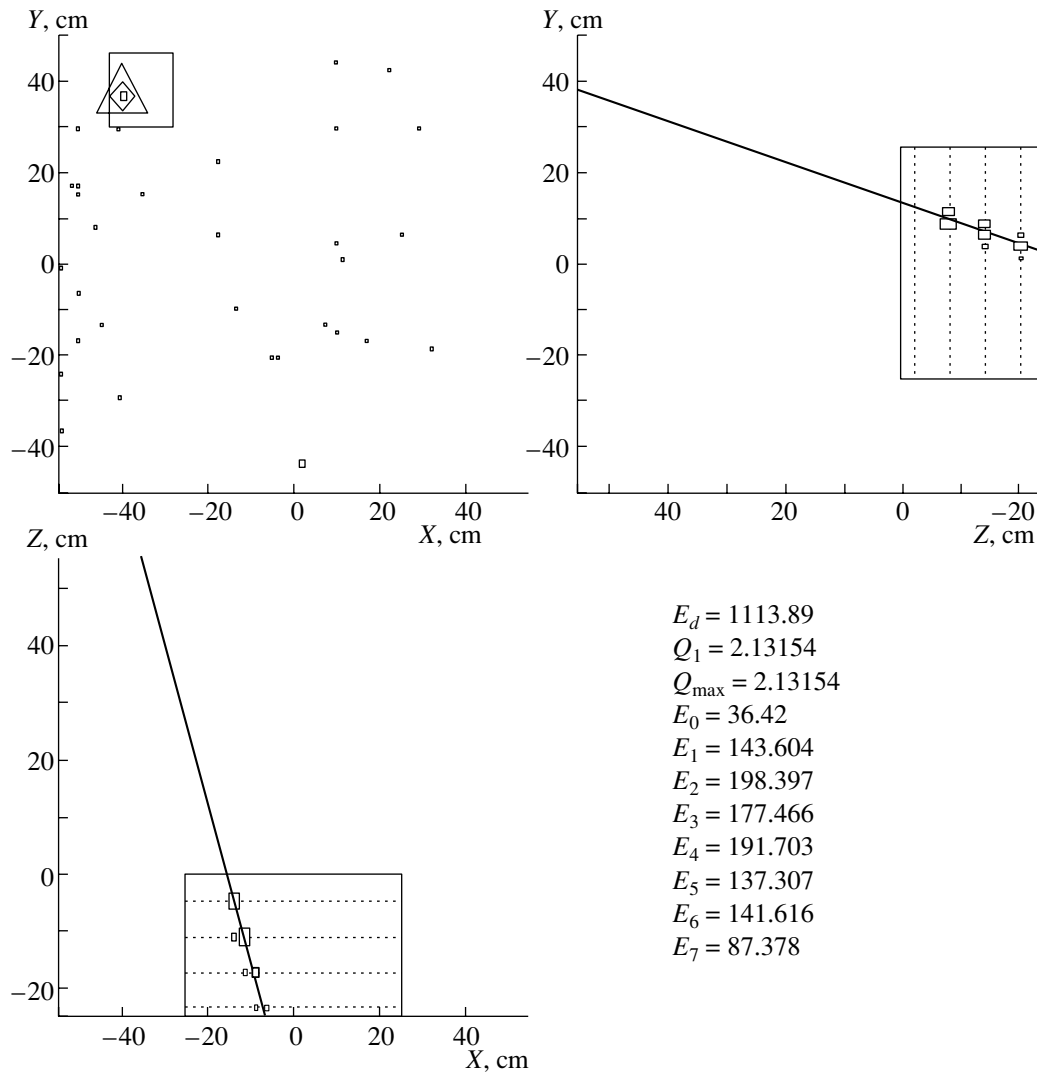


**Fig. 2.** Example of trajectory reconstruction and charge measurement for an event. The silicon matrix plane is shown in the upper left panel. The square delineates the search area; the triangle and the diamond indicate the locations of the detected charge and the maximum charge in the matrix, respectively.  $Q_1$  is the maximum charge in the search area,  $Q_{\max}$  is the maximum charge in the matrix,  $E_d$  is the energy deposition in the calorimeter, and  $E_0 - E_7$  are the energy depositions in the calorimeter layers (in GeV).

calorimeter. Subsequently, the trajectory projections are extended until they intersect the Si-matrix plane, and the rms errors in the coordinates of the points of intersection in the Si-matrix plane,  $\sigma_X$  and  $\sigma_Y$ , are determined. Then, the  $\pm 3\sigma_X$ ,  $\pm 3\sigma_Y$  area for primary particle search is delineated. The Si pixel with the maximum signal in the search area is selected, and the trajectory parameters are recalculated by taking into account the coordinates of the pixel center. The primary particle charge is determined from the formula  $Z = \sqrt{A \cos \theta}$ , where  $\theta$  is the zenith angle of the trajectory, and  $A$  is the signal in the Si pixel in MIPs (MIP is the energy deposition of a vertical minimum ionizing particle in a silicon pixel). For each reconstructed event, the energy deposition in the calorime-

ter  $E_d$  is calculated by adding the energy depositions of all crystals in all layers of the calorimeter. The signals in the scintillator hodoscopes were not used at this stage of our analysis.

Figure 2 shows an example of event reconstruction. Figure 3 shows the experimental distributions of the distances along the  $x$  axis from the cascade axis to the center of the pixel with the maximum signal for three energy ranges. The width of these distributions is seen to decrease with increasing primary particle energy, since the nuclear dispersion decreases in importance and the Coulomb electron scattering begins to play a major role in the lateral distribution. The rms errors of these distributions in each coordinate,  $\sigma_X$

and  $\sigma_Y$ , and the mean size of the  $\pm 3\sigma$  search area as a function of the cascade energy are given in Table 1.

## 5. EXPERIMENTAL DATA

About 25 million events were detected in the ATIC-1 experiment. For our analysis of the backscatter current, we selected 7000 events with energy deposition  $E_d > 10$  GeV and the same number of events with  $E_d > 100$  GeV as well as all events (about 1600) with  $E_d > 1$  TeV. When processing the raw data, in addition to information about the charge, energy deposition, and trajectory of the primary particle in these events, we recorded information about all signals in the silicon matrix. These signals, except the signal from the primary particle, were produced by the backscatter current or were noise signals. In Fig. 4, the number of albedo and noise signals in the entire matrix per event ( $n_a$ ) is plotted against the equivalent charge  $Q = \sqrt{A}$  for three ranges of energy deposition and three types of primary particles. The noise signals dominate at  $Q < 1$ , and their number does not depend on energy. On average, there were about 20 noise signals per event. The number of albedo signals decreases with increasing  $Q$  almost exponentially and increases with energy and charge of the primary particle. As the energy rises by an order of magnitude, the number of albedo particles increases by a factor of about 3.

## 6. SIMULATIONS

Initially, simulations were undertaken at the design stage of the instrument and were performed for the design with four 10-cm-thick graphite layers and for the silicon matrix with  $3 \times 3$ -cm pixels. For our simulations, we used the GEANT-3.21 software package, in which a hadron cascade was simulated using the FLUKA generator [9]. The primary particles were protons with energies of  $10^2$ ,  $10^3$ , and  $10^4$  GeV. The results of these simulations were published in [7]. Electrons (bearing in mind both electrons and positrons), pions, photons, and protons were shown to give the main contribution to the albedo signal in the matrix. The relative contribution of pions and, especially, protons increases with the albedo signal. It was also shown that, for a pixel size of  $3 \times 3$  cm, the frequency of events in which the albedo signal in the axis pixel exceeded 1 MIP is less than 1.5% even at an energy of 10 TeV; i.e., the albedo signals in the matrix are essentially separated from the primary particle signal.

We performed new simulations for the actual design of the instrument. An isotropic particle flux with a power-law energy distribution with index  $\gamma = 1.6$

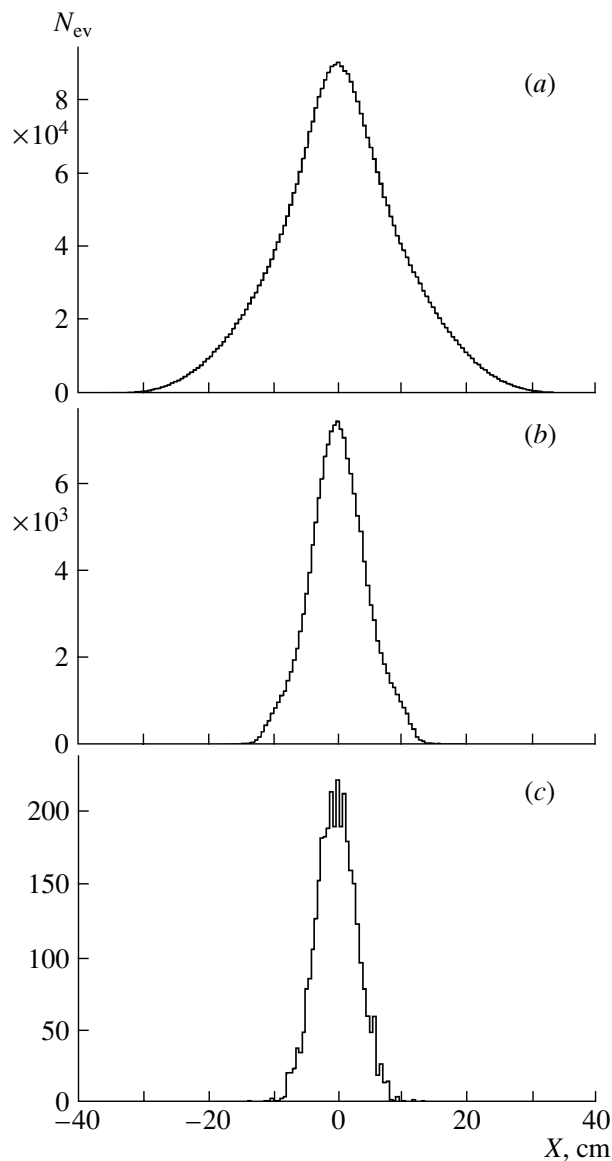


**Fig. 3.** Distribution of distances along the  $x$  axis from the primary particle location to the reconstructed trajectory: (a)  $E_d > 10$ , (b)  $E_d > 100$ , and (c)  $E_d > 1000$  GeV. The number of events ( $N_{ev}$ ) in the bin is along the vertical axis.

was incident on the silicon matrix plane over the aperture of the instrument. The simulations were carried out for three ranges of primary kinetic energies,  $E > 10$ ,  $>100$ , and  $>1000$  GeV, and cascades with energy deposition  $E_d > 10$ ,  $>100$ , and  $>1000$  GeV, respectively, were selected for the analysis. Protons and helium nuclei were taken as the primary particles. We used the QGSM generator [10] to simulate the interactions of helium nuclei. The statistics in our simulations were  $10^4$  cascades for protons and  $10^3$  cascades for helium in each energy range. To be

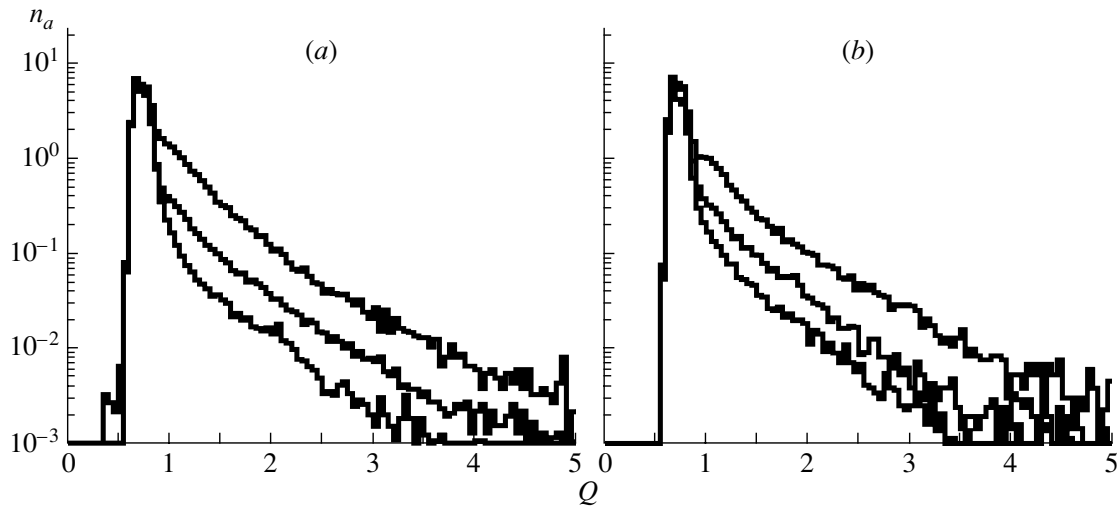


**Fig. 4.** Experimental albedo distribution in equivalent charge  $Q$  ( $n_a$  is the number of albedo signals per event in the entire matrix). (a) Three ranges of energy deposition:  $E_d > 1000$  (upper histogram),  $E_d > 100$  (middle histogram), and  $E_d > 10$  GeV (lower histogram); (b) three types of primary particles for  $E_d > 100$  GeV: nuclei with  $Z > 3$  (upper histogram), helium nuclei (middle histogram), and protons (lower histogram).

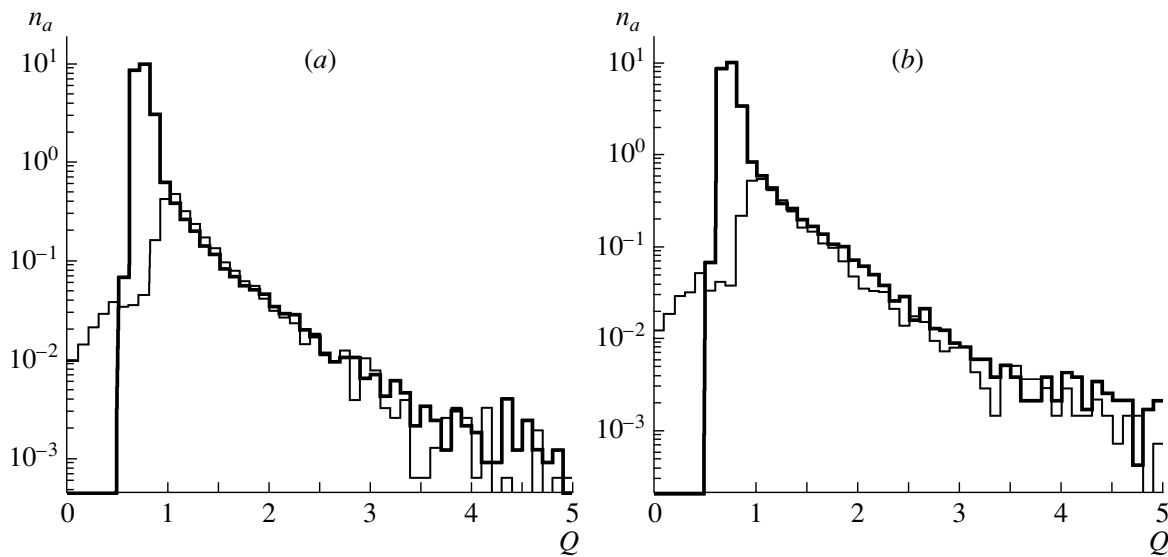


**Fig. 5.** Comparison of the experimental data with simulations ( $n_a$  is the number of albedo signals per event in the entire matrix for  $E_d > 100$  GeV): (a) protons and (b) helium nuclei. The thin line represents our simulations.

sure that the simulation results are valid, they must be compared with experimental data.

Figure 5 compares the experimental and simulated distributions of albedo signals in  $Q$  for  $E_d > 100$  GeV. We can see that the agreement is good at  $Q > 1$ , where the number of noise signals is negligible.

Figure 6 shows the simulated lateral distribution of albedo signals with  $Q > 1$  in the silicon matrix for protons with  $E_d > 100$  GeV. Also shown here is the experimental lateral distribution of albedo signals at

$R > 20$  cm. The albedo particle density at  $R < 20$  cm cannot be studied experimentally, since the maximum signal in this region (the search area) is considered as the signal from the primary particle. The region of  $R > 80$  cm can be distorted in the experiment, because large distances are associated with particles near the edge of the matrix. In this case, there is a probability that the axis of the cascade produced by the nucleus that past by the matrix could be restored inside the matrix, and the signal from the backscat-

**Table 3.** Distortions of the proton and helium-nucleus fluxes due to the albedo  $\delta_a$ , ionization loss fluctuations  $\delta_i$ , and their sum  $\delta$  (in %)

Row number	$\delta_a$			$\delta_i$			$\delta$		
	$E_d$ , GeV			$E_d$ , GeV			$E_d$ , GeV		
	>10	>100	>1000	>10	>100	>1000	>10	>100	>1000
1	-1.87	-2.29	-2.55	-3.68	-3.68	-3.68	-5.55	-5.97	-6.23
2	-0.47	-0.60	-0.90	-5.16	-5.16	-5.16	-5.63	-5.76	-6.06
3	+3.20	+2.39	+2.48	+7.80	+4.94	+4.19	+11.0	+7.33	+6.67
4	+2.73	+1.79	+1.58	+2.64	-0.22	-0.97	+5.37	+1.57	+0.61

Note: Row 1—decrease in proton flux, row 2—decrease in helium flux, row 3—increase in helium flux due to proton admixture, and row 4—sum of rows 2 and 3.

ter current of the nucleus could be mistaken for the proton signal. As we showed, the number of albedo signals from nuclei is larger than that from protons. Note that the values of albedo signal density  $D_a$  in the experiment and the simulations are not normalized to one another.

Thus, both the lateral distribution of albedo signals and their  $Q$  distribution are satisfactorily reproduced by the simulations. Therefore, we will use the results of our simulations for the subsequent analysis of the albedo influence when determining the charge from the maximum signal in the search area.

## 7. CHARGE RESOLUTION IN THE ATIC EXPERIMENT

To estimate the albedo influence, we must calculate the probability that the albedo signal rather than the signal from the primary particle will be the maximum signal in the search area, and, thus, the primary particle will be misidentified. Table 2 gives the calculated probabilities of detecting backscatter signals with  $Q > 1.5$  for protons and  $Q > 2.5$  for helium nuclei for three sizes of the search area and three ranges of energy deposition. Table 3 gives the distortions of the protons and helium fluxes due to the albedo  $\delta_a$  when using the algorithm of primary particle search employed in the experiment for simulated events. For protons and helium, the flux is shown to decrease, because the measured charge  $Q$  exceeds 1.5 and 2.5, respectively (rows 1 and 2). The admixture to the helium flux from protons is given in row 3 (for this estimate, the relative number of cascades from protons and helium in the experiment was taken into account), and row 4 gives the total effect for helium in the range  $1.5 < Q < 2.5$ .

In addition to the albedo, the fluctuations of ionization losses in the silicon detector are another process that leads to misidentification of protons and helium nuclei. The fluctuations of ionization losses in the silicon detector of the ATIC instrument were analyzed in [8]. The distortions of the proton and helium fluxes due to this process  $\delta_i$  and the total distortion  $\delta = \delta_a + \delta_i$  are also given in Table 3. We see from this table (row 2) that the decrease in the helium flux is determined mainly by the ionization loss fluctuations, not by the albedo particles.

The experimental proton and helium charge res-

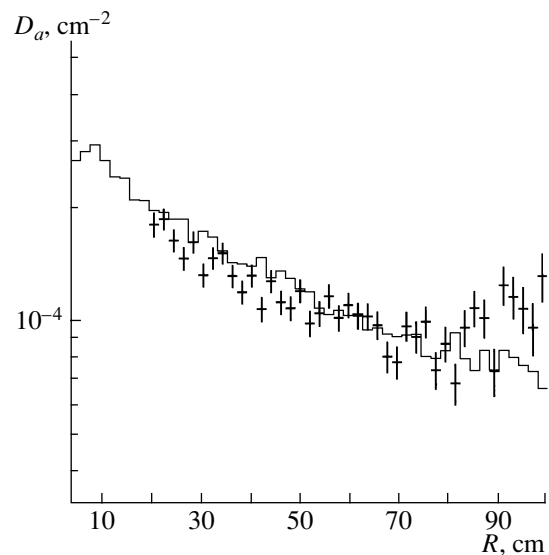


**Fig. 6.** Lateral distribution of the albedo signals from protons with  $E_d > 100$  GeV in the silicon matrix. The points with error bars represent the experimental data, and the histogram represents the simulations.

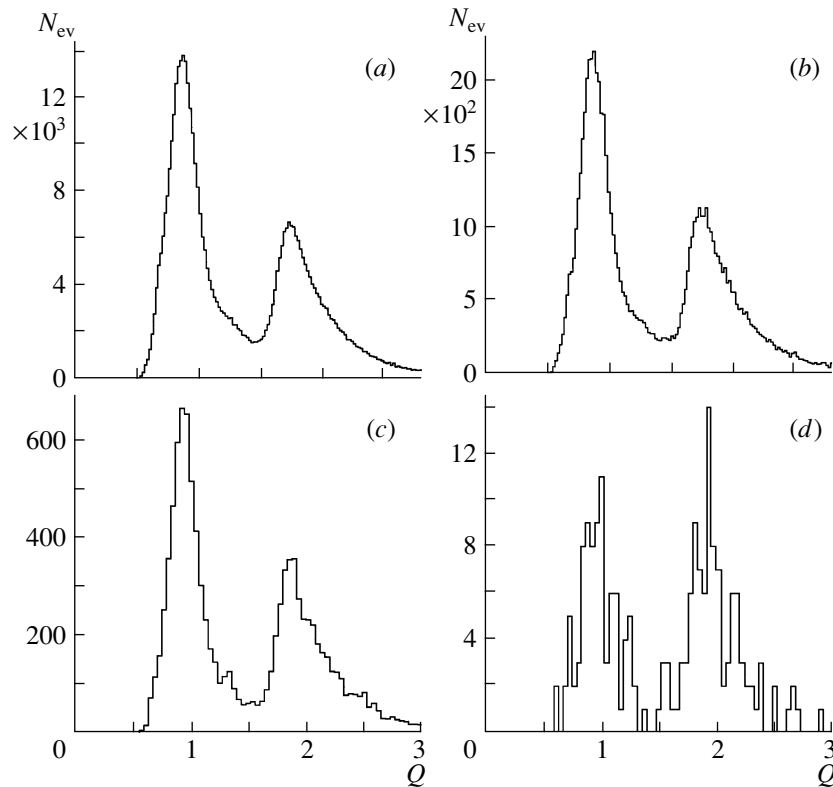


**Fig. 7.** Charge resolution for protons and helium nuclei in the experiment for four ranges of energy deposition: (a)  $50 < E_d < 150$  GeV, (b)  $150 < E_d < 500$  GeV, (c)  $500 < E_d < 5000$  GeV, and (d)  $E_d > 5000$  GeV. The number of events ( $N_{ev}$ ) in the bin is along the vertical axis.

olution is shown in Fig. 7 for four ranges of energy deposition.

## 8. CONCLUSIONS

The silicon matrix in the ATIC spectrometer has solved the problem of the backscatter current in this experiment and allowed a good charge resolution to be achieved for protons and helium and, consequently, the energy spectra of these particles to be measured. The required corrections to the measured proton and helium fluxes do not exceed 7%.

## ACKNOWLEDGMENTS

This work was supported in Russia by the Russian Foundation for Basic Research (project nos. 02-98-16246 and 02-02-16545) and in the United States by NASA (grant nos. NAG5-5064, NAG5-5306, NAG5-5155, and NAG5-5308).

## REFERENCES

1. N. L. Grigorov, G. P. Kakhidze, I. D. Rappoport, *et al.*, *Kosm. Issled.* **5**, 38 (1967).
2. R. W. Ellsworth *et al.*, *Nucl. Instrum. Methods Phys. Res.* **203**, 167 (1982).
3. V. I. Zatsepin, E. A. Zamchalova, A. Ya. Varkovitskaya, *et al.*, in *Proceedings of the 23rd ICRC, Calgary, 1993*, Vol. 2, p. 13; V. I. Zatsepin, T. V. Lazareva, G. P. Sazhina, and N. V. Sokol'skaya, *Yad. Fiz.* **57**, 684 (1994) [*Phys. At. Nucl.* **57**, 645 (1994)].
4. K. Asakimori *et al.* (JACEE Collab.), *Astrophys. J.* **502**, 278 (1998).
5. A. V. Apanasenko *et al.* (RUNJOB Collab.), *Astropart. Phys.* **16**, 13 (2001).
6. N. L. Grigorov, *Yad. Fiz.* **51**, 157 (1990) [*Phys. At. Nucl.* **51**, 99 (1990)].
7. J. H. Adams, Jr., G. L. Bashindzhagyan, V. I. Zatsepin, *et al.*, *Prib. Tekh. Éksp.* **44** (4), 38 (2001) [*Instrum. Exp. Tech.* **44** (4), 455 (2001)].
8. V. I. Zatsepin, J. H. Adams, Jr., *et al.*, *Nucl. Instrum. Methods Phys. Res. A* **524**, 195 (2004).
9. R. Brun, F. Brayant, M. Maire, *GEANT Users Manual*, CERN DD/EE/84-1 (Geneva, 1984); <http://wwwasd.web.cern.ch/wwwasd/cernlib>
10. I. D. Rappoport, A. N. Turundaevskii, and V. Ya. Shestoporov, *Yad. Fiz.* **65**, 176 (2002) [*Phys. At. Nucl.* **65**, 170 (2002)]; N. S. Amelin, K. K. Gudima, and V. D. Toneev, *Yad. Fiz.* **51**, 512 (1990) [*Sov. J. Nucl. Phys.* **51**, 327 (1990)].

*Translated by V. Astakhov*